Lattice Rotations in Precipitate Free Zones in an Al-Mg-Si Alloy[☆]

Emil Christiansen[a,b,*], Calin Daniel Marioara[a,c], Knut Marthinsen[a,d], Odd Sture Hopperstad[a,e], Randi Holmestad[a,b]

[a]*Centre for Advanced Structural Analysis (CASA), NTNU, N-7491 Trondheim, Norway*
[b]*NTNU, Department of Physics, Høgskoleringen 5, N-7491 Trondheim, Norway*
[c]*SINTEF Industry, N-7465 Trondheim, Norway*
[d]*NTNU, Department of Materials Science and Engineering, Alfred Getz vei 2, N-7491 Trondheim, Norway*
[e]*NTNU, Department of Structural Engineering, Richard Birkelands vei 1a, N-7491 Trondheim, Norway*

Abstract

Scanning precession electron diffraction and automated crystal orientation mapping in a transmission electron microscope (TEM) have been applied to quantitatively study the crystal orientation of precipitate free zones (PFZs) of four GB regions in an AA6060 alloy in peak aged condition (temper T6) after uniaxial compression to 20% engineering strain. The PFZ width in the alloy is found to be $w = 170 \pm 40\,\mathrm{nm}$. The results show that some PFZs develop significant misorientations relative to their parent grain, and represent, to the best knowledge of the authors, the first quantitative evidence of this. This misorientation may either be constant inside a particular PFZ, making it appear like a band or a very elongated subgrain, or be partitioned in discrete regions with a diameter comparable to the PFZ width, making the former PFZ into a collection of small grains. The band-like PFZ observed in this work had a misorientation relative to its parent grain of $\sim 7°$, while the grain-like PFZ had grains with misorientations between $\sim 12°$ and $\sim 20°$ relative to its parent grain. The other PFZs that were observed had only limited misorientations relative to their parent grains, and had either dislocations perpendicular to the GB plane or a dislocation wall at the transition region. A general TEM study of the material at various engineering strains was also conducted and suggests that grain-like PFZs are more frequent for larger strains, indicating that the different PFZ features are likely due to different strain localisation in individual PFZs. This localisation is expected to be influenced by the orientation of the loading axis relative to crystal orientations and GB planes. It is also suggested that the different PFZ features engender different work hardening rates and possibly affect nucleation of intergranular fracture. The results support previous studies on the microstructure evolution of PFZs in age-hardenable aluminium alloys during deformation.

Keywords: aluminium, deformation, transmission electron microscopy, scanning precession electron diffraction, precipitate free zones.

1. Introduction

Precipitate free zones (PFZs) along grain boundaries (GBs) in age-hardenable aluminium alloys and their relation to material properties have been studied for many years [1–5]. The review by Vasudévan and Doherty [5] covers the earlier works on the topic and concludes that, while particles and precipitates on GBs are the most important sites for nucleation and growth of intergranular ductile fracture, PFZs also serve their part by localising strain and accelerating void nucleation and growth at the GB particles. PFZs form due to vacancy and/or solute diffusion to grain boundaries [6], where solute form precipitates and particles, while at the same time the precipitation potential in the PFZ is suppressed. Whereas small metastable precipitates that form homogeneously throughout the grain are beneficial to strength [7], these GB precipitates and particles can be detrimental to ductility [5]. Because the PFZ lacks hardening precipitates, strain may localise in these regions and thus promote intergranular fracture. This is especially true for GBs inclined to the loading direction so that the shear stress along their PFZs becomes large [8]. However, since the PFZs typically retain some solute in solid solution [6], they will be stronger than pure aluminium [9]. It is clear that the material behaviour depends on the width and work hardening of the PFZs, the GB precipitation, and the grain interior strength, which makes it challenging to isolate influences from individual parameters. Because of this complexity, both experiments and simulations are necessary in order to elucidate the impact of each parameter. This work is an experimental study of lattice orientations inside PFZs of an Al-Mg-Si alloy after deformation. No attempt is made to provide direct information regarding the influences of different parameters, but rather to provide insight into the strain localisation in the PFZs in an age-hardenable aluminium alloy. Such insight should prove relevant for simulations such as the ones by e.g. Pardoen *et al* [10, 11] that establish continuum models with assumptions based on microstructural knowledge.

A study by Schwellinger [4] showed that PFZs in Al-Mg-Si alloys may develop misorientations of ∼ 20° relative to their parent grains when such alloys were strained close to fracture. He observed walls with large dislocation densities at the PFZ boundaries (i.e., the interface between PFZ and precipitate strengthened grain), and suggested that these may serve as void initiation sites when impinged by slip bands from the grain interiors. This suggestion was motivated by observations of Gardner *et al* [12] and Wilsdorf *et al* [13] who showed how dislocation structures can serve as nucleation sites for voids in pure metals. More recent studies on pure tantalum crystals support this idea, and attribute such void formation to vacancy condensation at dislocation cell boundary block walls [14]. Although void nucleation and growth in precipitate strengthened alloys will be different from that in pure metals, it seems reasonable that dislocation structures should have some impact on ductile fracture.

In addition to Schwellinger [4] there are several studies that have reported on dislocation structures in PFZs of aluminium alloys [15–18]. Styczyńska *et al* [15] observed by *in situ* TEM straining experiments that dislocation sources at GBs became active before sources inside the grain interiors. This resulted in

dislocations bowing out from the GB and becoming pinned at the precipitates at the PFZ boundary, before penetrating into the grain interiors. During cyclic loading, Jain [16] observed dislocation networks within grains that terminated at the outer edges of the PFZs. He also observed dislocation structures inside the PFZs similar to those observed by Schwellinger [4]. Watanabe *et al* [17] did not study PFZs specifically, but noted that some PFZs in an Al-Mg-Sc alloy under cyclic loading became misoriented relative to their parent grains. Khadyko *et al* [18] observed several different dislocation structures in PFZs and their vicinity in an Al-Mg-Si alloy stretched to fracture in uniaxial tension. In most PFZs, both inside and outside the neck, dislocations spanned the PFZs and appeared almost perpendicular to the GB plane. Inside the neck however, some GB PFZs were misoriented relative to their parent grains, or had dislocation walls along their PFZ boundaries. Khadyko *et al* [18] also performed crystal plasticity simulations taking the dislocation storage close to PFZs into account, and observed an increased stress and strain localisation within PFZs compared to a model with no PFZ, as well as a lattice rotation within the PFZs. Such effects were larger for PFZs inclined to the loading axis. Even though misoriented PFZs have been observed in strained aluminium alloys for the last 35 years, and several hypotheses exist regarding their importance, the only work attempting to quantify such misorientations is the one by Schwellinger [4]. With the advent of more advanced techniques, it is now possible to investigate the misorientations in greater detail. Therefore, the aim of the present study is to determine crystal orientations within PFZs along grain boundaries in an age-hardenable aluminium alloy.

Quantification of crystal lattice orientations is possible on the nanoscale by automated crystal orientation mapping [19] of scanning precession electron diffraction (SPED) [20, 21] data. This technique is perfect for studying orientations within PFZs because it can be combined with a conventional TEM study of the exact same region. This means that imaging, dislocation analysis, and crystal orientation mapping can be performed from the same GB region and neighbourhood.

The alloy used in this study is the lean Al-Mg-Si alloy AA6060. When this alloy is heat treated, small metastable precipitates form homogeneously inside the grains through vacancy and solute condensation from a super saturated solid solution and subsequent growth [22–24]. The main hardening precipitate phase in this alloy system is the β'' precipitate, which forms as long needles along the $<100>$ directions of the aluminium matrix in the peak aged condition (T6 temper) [25]. This precipitate phase has a monoclinic unit cell with $a = 1.516$ nm, $b = 0.405$ nm, $c = 0.674$ nm, and angle $\beta = 105.3°$ [26]. The needles are coherent with the matrix along their length, and strain their local matrix neighbourhood in their lateral dimensions [27]. This alloy has been used in several other studies, including Khadyko *et al* [18] and Frodal *et al* [28], and serves as a model alloy, which also has extensive industrial applications. We have deformed the alloy in compression in order to examine a wide range of strains, which would not be possible in tension. A general TEM investigation of PFZs of several GBs in specimens compressed to 5%, 10%, 20%, and 50% engineering strains has been conducted to investigate the variety of PFZ microstructures that forms. The

study focuses, however, on a detailed SPED and orientation mapping study of crystal orientations inside PFZs of four individual GBs in the specimen compressed to 20%, and how these GB PFZs relate to the general observations.

2. Materials

The material used in this work was an extruded profile of the AA6060 aluminium alloy. The composition of the alloy is given in Tab. 1. Small cylinders measuring 9 mm in diameter and 13 mm in length were machined from the profile with their longitudinal direction along the transverse direction (TD) of the profile, see Fig. 1. The cylinders were subjected to a standard T6 heat treatment as illustrated in Fig. 2. The exact same alloy and heat treatment was studied by Frodal et al [28], where it was found that the material had an equiaxed and recrystallized grain microstructure. The grain size is approximately 60 µm to 70 µm.

Table 1: Nominal composition of the AA6060 alloy in wt% and at%.

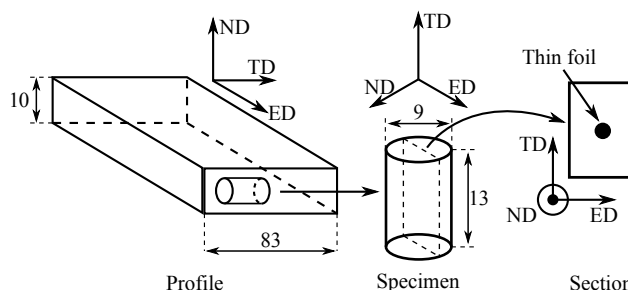|	Fe	Si	Mg	Mn	Cr	Cu	Zn	Ti	Al
wt%	0.193	0.422	0.468	0.015	0.000	0.002	0.005	0.008	Bal.
at%	0.093	0.406	0.520	0.007	0.000	0.001	0.002	0.005	Bal.

Figure 1: Sketch of compression specimen geometry. The extruded profile coordinate system is shown: extrusion direction (ED); transverse direction (TD); and the normal direction (ND). Cylindrical specimens were machined from the extruded profile with longitudinal axes along the TD. Sections of the TD-ED plane were cut from the approximate middle of the cylinders after compression, and TEM thin foils were prepared from various locations of the section. Measures are in mm. Not to scale.

Uniaxial compression tests of the cylinders along their longitudinal axis were done in a universal testing machine with a constant crosshead speed of approximately 0.15 mm/ min, corresponding to a strain rate of $2 \times 10^{-4}\,\mathrm{s}^{-1}$, to 5%, 10%, 20%, and 50% compressive engineering strain. In order to limit friction between the specimens and compression platens, the contact surfaces were lubricated with *Dow Corning Molykote G-n Metal Assembly Paste*. The degree of barrelling was less than 6% in all tests. Due to the anisotropy of the material, the aspect ratio of the specimens changed during compression, and in the most severe case (i.e.,
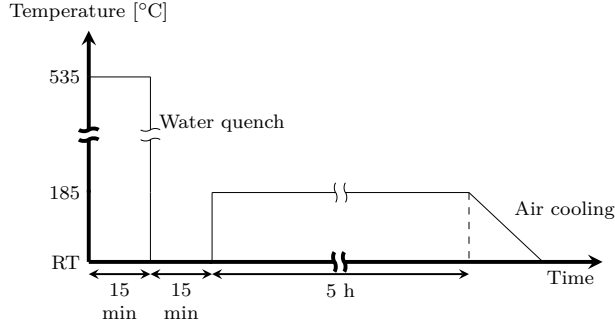
Figure 2: Sketch of the alloy heat treatment. The specimens are solution heat treated at 535 °C for 15 min in a salt bath and quenched to room temperature (RT) in water, before being naturally aged for 15 min at RT with subsequent artificial ageing for 5 h at 185 °C in an oil bath. At the end of artificial ageing, the specimens are cooled to RT in still air.

at 50% engineering strain) the aspect ratio between the extrusion direction (ED) and the normal direction (ND) of the cylinders was ∼ 1.4. Results presented in this work are from undeformed and 20% compressed specimens, but observations from the other compression levels are mentioned and discussed as well. The SPED and orientation mapping results presented here are from a single TEM thin foil to ensure that the macroscopic strain of the GBs studied is roughly the same. In order to compare PFZ microstructures of different GBs, the study is limited to high angle grain boundaries (HAGBs).

Sections containing the TD and extrusion direction (ED), i.e. the TD-ED plane, of the compression specimens were cut close to the specimen centres as indicated in Fig. 1. These sections were mechanically polished down to a thickness of ∼200 µm to ∼300 µm before 3 mm disks were cut out. The compression axis (CA) of the specimens was marked by cutting notches on opposite sides of each disk using a scalpel, before they were polished further on both faces down to a final thickness of 50 µm to 120 µm. Electropolishing was done in a *Struers Tenupol 3* unit operating at 20 V using a mixture of $^1/_3$ HNO$_3$ (Nitric acid) and $^2/_3$ CH$_3$OH (Methanol) as electrolyte, which was kept at -25 ± 5 °C. The orientation of the CA in TEM images was determined by imaging the thin foils and their CA notches through a visible light microscope after inserting them in the TEM holder, and correcting for image rotations in the TEM. The errors in CA orientation are estimated to be in the order of $\pm 5°$.

TEM investigations were carried out on three different instruments. A double tilt holder and a *Philips CM30* with a LaB$_6$ filament operating at 150 kV equipped with film and a *Gatan PEELS model 601* were used for precipitate statistics using the method in [25, 29]. For bright-field (BF) and weak-beam dark-field (WBDF) studies of deformed microstructures, a LaB$_6$ *JEOL JEM2100* with an accelerating voltage of 200 kV was used with a double tilt holder. Measurement of the PFZ width w was conducted on images from this microscope by measuring the shortest distance from the GB to the first intersection with a precipitate at 64 equidistant points along the GB and taking the average. WBDF imaging was performed close to the conventional $\vec{g} - 3\vec{g}$ diffraction condition with the diffracted beam along the optical axis by first tilting the

5

specimen to a two-beam condition for $\vec{g}$ and subsequently tilting the incoming electron beam so that the $\vec{g}$ diffracted beam travelled along the optical axis. The tilt of the electron beam also caused $3\vec{g}$ to excite, leaving $\vec{g}$ weak with a positive excitation error and suitable for WBDF imaging. Finally, an in-plane rotation holder with single tilt and a *JEOL JEM2100F* operating at 200 kV equipped with a *NanoMEGAS DigiSTAR* system were used to perform SPED [20, 21] with a spot size of 1.0 nm and a nearly parallel beam. Deflector coils above the specimen were used to precess the beam around the optical axis with an angle of 1.0° and a frequency of 100 Hz. Another set of coils below the specimen counteracts the precession, giving the same result as that of precessing the specimen in a stationary beam. In diffraction, this gives a precession electron diffraction pattern (PED) which can be considered equivalent to an electron diffraction spot pattern that is averaged through several incoming beam directions. Thus, more of the reciprocal space of the crystal is probed, and dynamical diffraction effects are somewhat reduced. This probe was then scanned across the specimen in a 320×640 pixel raster with step length 3.2 nm resulting in a rectangular scan region of 1024×2048nm^2. At each probe position, a PED pattern was acquired. Acquisition of the PED patterns was done by illuminating the microscope phosphorous screen (tilted 30°) and acquiring images of this by an external Allied StingRay CCD camera with 144×144 pixels and 8-bit depth. The exposure time was 40 ms and synchronized with the scan dwell time. Each grain boundary was aligned along the tilt axis of the rotation holder and oriented edge-on to the optical axis. For each SPED scan, the slow scan direction was aligned along the GB. Due to the slow decay of the phosphorous screen, afterglow caused the spots in the last diffraction patterns of a line to remain significant in the diffraction patterns of the next line. Therefore, the first 20 pixels (64 nm) of each line were removed as indicated in Fig. 3, and are not present in the misorientation maps. Afterglow effects are present in the remaining pixels as well, and will influence the appearance of features in the scan. However, due to the long exposure time and small step size, this afterglow effect is not detrimental to the technique.
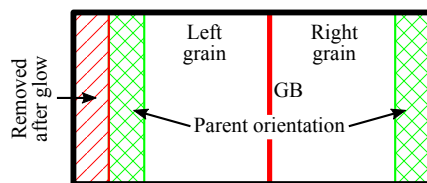

Figure 3: Illustration of SPED map and regions used for parent grain orientation calculations. The first 20 pixels (64 nm) of each line are removed due to afterglow effects and are shown as the red hashed area. The mean orientation of a region 20 pixels wide on each side (shown as green square-hashed regions) is used as a reference for that particular parent grain when calculating misorientation angles. Size of raw data scan is 1024×2048 pixels, and only a part of a full scan is illustrated. Not to scale.

Orientation mapping based on the 4D SPED data was performed by matching each PED pattern of the SPED stacks to a bank of simulated Al spot diffraction templates by the commercial *NanoMEGAS*

ASTAR Index package. The procedure is explained in detail by Rauch and Véron [19]. The resulting data set consists of crystal Euler angles, the cross-correlation index between each experimental pattern and its matched template, and the reliability of each match. In this work, accepted matches for each PED pattern have at least 15% higher cross-correlation index than the second best match of that particular PED pattern, and a cross-correlation index of at least 15.0. These thresholds have been somewhat arbitrarily chosen, but are motivated by the fact that both of these values should be reasonably high for a good match. SPED frames with matches not fulfilling these criteria are not analysed, and appear white in the misorientation maps. The quality of orientation mapping results was controlled by comparing regions of low cross-correlation index and reliability to the raw data in the SPED stack.

The *MATLAB* open source toolbox *MTEX* [30] was used to analyse the orientation mapping results. For each SPED scan, the orientation of the left-hand side and right-hand side "parent grains" were calculated by averaging the orientations within narrow regions (64 nm wide) along the left-hand side and right-hand side of the scan, respectively. These regions are illustrated in Fig 3. These parent orientations serve as a reference, and the orientations on either side of the GB are compared to their respective parent grains to calculate misorientation maps. To make comparisons between the misorientation maps easier, the misorientation scalebars for each misorientation map are the same, and the minimum and maximum values correspond to the overall minimum and maximum values of measured misorientation angle. Pole figures are in stereographic projection, and all orientations in the corresponding misorientation map are included. Note that the pole figures only show the orientations on either side of the grain boundaries in relation to each other, and should not be correlated to the specimen or scan coordinate axes.

3. Results

TEM studies of the alloy in the undeformed state were performed to establish a reference for the investigation of the deformed states. Fig. 4 presents TEM images of the microstructure of the alloy prior to deformation. The characteristic diffraction contrast of β'' precipitates is clearly seen in the BF image. The precipitates are oriented with their longitudinal axis along <100> directions and appear as needles along [010] and [001], while the ones along [100] are aligned out-of-plane and appear as dots. When imaged in high resolution TEM (HRTEM), these cross sections show the β'' crystal periodicity. All cross-sections observed were consistent with the β'' crystal structure [26]. From several images similar to the ones presented in Fig. 4a and Fig. 4b, as well as thickness measurements using electron energy loss spectroscopy, the average needle length, cross-section area, number density, and volume fraction were estimated to be $\bar{l} = 40 \pm 1\,\text{nm}$, $\bar{\sigma} = 19.1 \pm 0.8\,\text{nm}^2$, $\bar{\rho} = 5556 \pm 629\,\#/\mu\text{m}^3$, and $\bar{V}_f = 0.42 \pm 0.05\,\%$, respectively. The BF TEM image of a HAGB presented in Fig. 4c shows a characteristic GB PFZ in the undeformed state. Measurements of the PFZ widths of three different GBs resulted in a mean PFZ width of $w = 170\,\text{nm}$ with a standard deviation

of 40 nm. This standard deviation serves as an estimate of the width of the transition zone between PFZ and the grain interior. PFZ widths of both HAGBs and low angle GBs (LAGBs) were measured, and no large variations in PFZ width were observed.
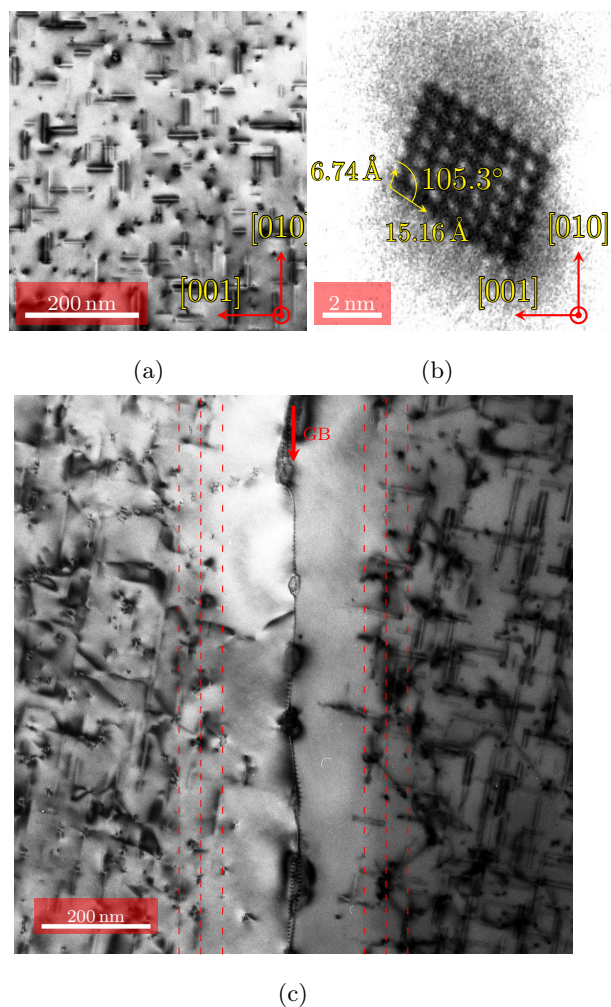

(a)

(b)

(c)

Figure 4: Microstructure of the undeformed alloy. In a) the BF TEM image shows the precipitates along [001] and [010] in aluminium as sets of two parallel lines of strain contrast and the precipitates along [100] as dots. In b) the HRTEM image of one cross-section is shown, with parameters for the β″ phase overlaid [26]. Both a) and b) were acquired in the [100] zone axis of aluminium. Subfigure c) shows a representative HAGB with PFZs on either side. The GB is marked by a red arrow, and the PFZ width $w = 170$ nm with its standard deviation of 40 nm are marked by dashed lines.

Based on conventional BF TEM investigations of the deformed states, four main features of the deformed PFZ microstructure were defined. These are "perpendicular dislocations" that span the PFZ, "dislocation walls" in the transition regions, "PFZ misorientation bands", and "PFZ grains", from now on referred to as (in italic) *dislocations*, *walls*, *bands*, and *grains*, respectively. Specimens compressed 20% or more contain all four features, while the less deformed specimens only exhibit *dislocations*, *walls*, and *bands*. Results from

a detailed investigation using TEM and orientation mapping SPED of four GBs in a thin foil from a 20% compressed specimen are presented in the following and summarized in Table 2.

Table 2: Summary of the SPED orientation mapping results for the four HAGBs presented in Fig. 5 to 8 from a specimen deformed to 20% engineering strain. The CA-GB angle Φ and GB misorientation angle ϕ for each GB are given, along with the maximum misorientation θ, and observed features for either side of the GBs

Figure	Φ [°]	ϕ [°]	Side	θ [°]	Feature
Fig. 5	−66	24	Left	1.3	*Dislocations*
			Right	1.9	*Dislocations*
Fig. 6	64	21	Left	3.8*	*Dislocations*
			Right	5.8*	*Wall*
Fig. 7	16	28	Left	7.6	*Band*
			Right	3.0	*Wall*
Fig. 8	45	38	Left	20.0	*Grains*
			Right	11.6	*Grains*

* The misorientation values inside the relevant PFZ areas are much lower than the maximum value. Relevant values are $\sim 1°$, and $\sim 2.5°$, for the left-hand and right-hand side respectively.

Figure 5 presents WBDF, BF, and orientation mapping data from a HAGB (parent-parent misorientation $\phi = 24°$ and CA-GB angle $\Phi = -66°$) exhibiting PFZs with perpendicular dislocations, i.e. the *dislocations* feature, on both sides. The dislocation density inside the PFZs is much lower than in the grain interiors. As can be seen from the WBDF and BF images, the projected image-plane traces of the few dislocations inside the PFZ have relatively high angles relative to the projected GB trace. Thus, the dislocations appear to be oriented perpendicularly to the GB plane. However, the true three dimensional orientation of the dislocations could not be established. In the WBDF image in Fig. 5a the dislocations in the left-hand side PFZ are investigated. These dislocations can be divided into two groups, "b1" and "b2", based on their orientation relative to the GB plane. Other PFZs with the *dislocations* feature show similar tendencies. Different $\vec{g} - 3\vec{g}$ conditions were investigated, and the "b1" dislocations satisfy the invisibility criterion $\vec{g} \cdot \vec{b} = 0$ when $\vec{g} = [0\bar{2}2]$ is imaged, using the indexing of the inset diffraction pattern in Fig. 5a. Similarly, the "b2" dislocations disappear when $\vec{g} = [0\bar{2}\bar{2}]$ is used as imaging condition. Therefore, the dislocations in the "b1" group have $\vec{b} \parallel [x_1 11]$ and the ones in the "b2" group have $\vec{b} \parallel [x_2 \bar{1}1]$, where x_1 and x_2 are unknown Miller indices as only one invisibility condition was found for each set. Thus, the dislocations in "b1" have different Burgers vectors than the ones in the "b2" group. Furthermore, it is likely that all the dislocations in

each group have the same Burgers vector. Hence it is clear that the PFZ contains relatively few dislocations, and these dislocations can be separated into sets of different orientation and Burgers vector. Burgers vector analysis was not performed for other PFZs with the *dislocations* feature. Regarding the crystal orientation mapping results, it is clear that misorientation variations between the PFZs and their parent grain interiors are very small. This is also easily seen from the pole figure data, where the orientation measurements for each grain are concentrated to very small areas.

Figure 6 presents data for a HAGB (parent-parent misorientation $\phi \sim 21°$ and CA-GB angle $\Phi = 64°$) where the PFZ on the left-hand side contains *dislocations*, while the PFZ on the right-hand side displays a *wall*. In the BF TEM image, the *wall* is visible as a relatively sharp contrast change from the precipitate hardened grain interior to the PFZ. Correspondingly, there is a sharp misorientation change of $\sim 2° - 3°$ at this boundary in the misorientation angle map. Such an abrupt change in misorientation angle indicates a local concentration of tangled dislocations. The pole figures indicate a slightly larger variation of orientations in the right-hand side grain than in the other grain.

Figure 7 presents results from a HAGB (parent-parent misorientation $\phi = 28°$ and CA-GB angle $\Phi = 16°$) with a *band* on its left-hand side, clearly seen as contrast in the BF image. Indeed, the misorientation map shows that this PFZ has developed a misorientation of 4.5° to 7.0° relative to its parent grain. In the PFZ on the other side of the GB, a *wall* is present (not visible under the particular conditions of the BF image), giving this PFZ a misorientation of $\sim 2°$. The distinction between a *wall* and a *band* is somewhat diffuse, as both features are very similar. However, a PFZ with a *band* has larger misorientations than a PFZ with a *wall*. While a PFZ with a *wall* feature is misoriented 2° to 3°, a PFZ with a *band* feature is misoriented 4.5° to 7.0°. Additionally, the boundary between the PFZ and the grain interior tends to be sharper for a *band* than a *wall*. The pole figures show the greater variation of orientations in the left-hand side grain compared to the right-hand side grain.

Results from a HAGB (parent-parent misorientation $\phi = 38°$ and CA-GB angle $\Phi = 45°$) exhibiting the last feature, PFZ *grains*, are presented in Fig. 8. The GB interface appears jagged and is not as straight as for the other GBs presented previously. It can be seen from the BF TEM image that there are regions of different contrast within the PFZ to either side of the GB. In the misorientation map, these regions show large misorientations relative to their parent grains. For the right-hand side, regions of significant misorientations are present only in the lower part of the PFZ, with misorientations close to 0° at the top, and 3°, 6.5°, 8.5°, and 11°, sequentially down along the PFZ. The PFZ on the other side of the GB contains only regions of high misorientation, with values ranging from 12° to 20°. In addition, there are some regions with 10° misorientation that appear more than 200 nm from the GB, indicating that they have formed just outside the PFZ. Boundaries between regions are very sharp in the left-hand side PFZ, while they are more diffuse in the other. However, in all cases the interface between the PFZ grains and the parent grain is very sharp. The variations in orientations are very clear in the pole figures as well, where the left-hand side has
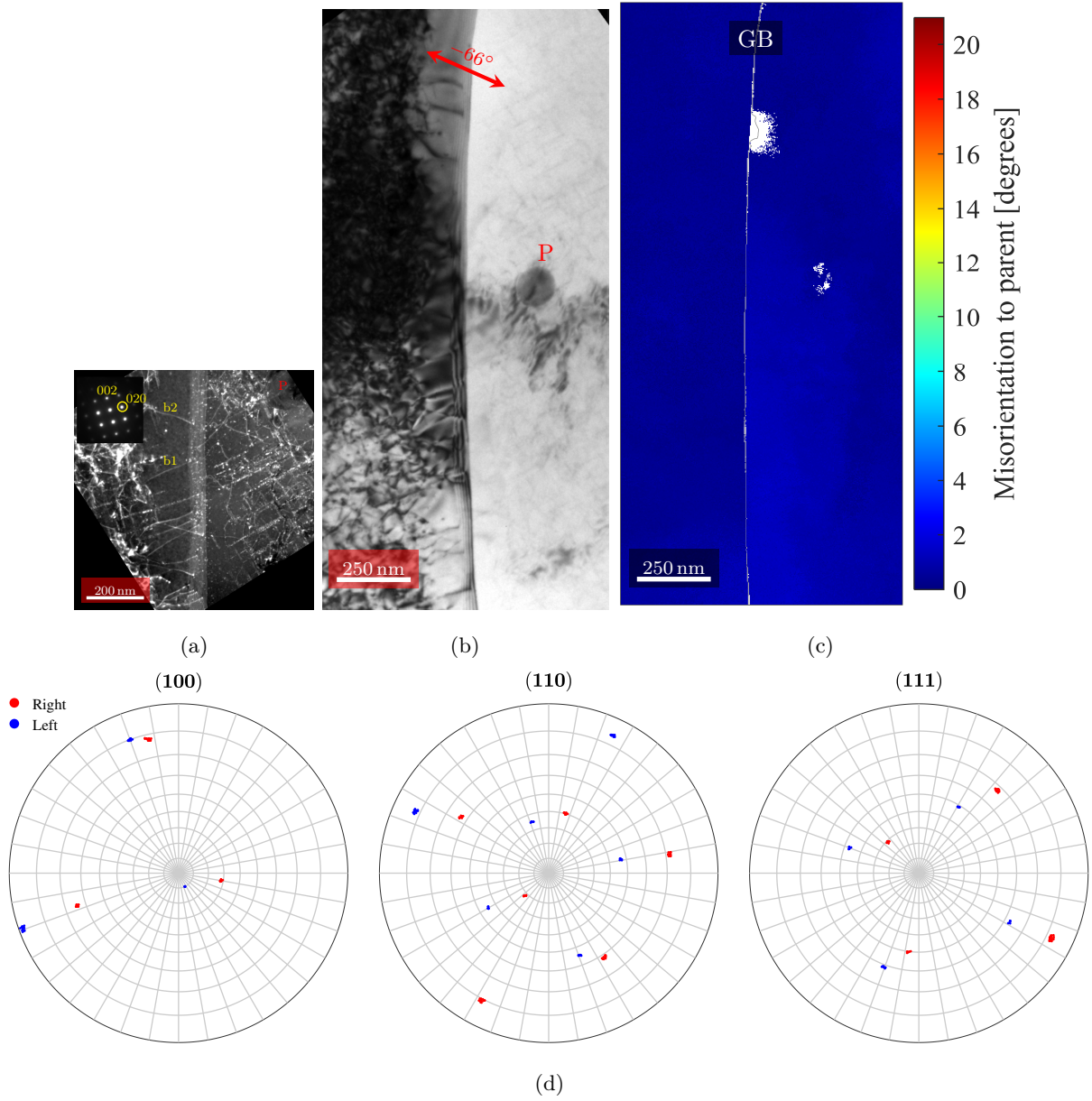
(a) (b) (c)

(100) (110) (111)

● Right
● Left

(d)

Figure 5: PFZs exhibiting *dislocations*. The parent-parent misorientation is $\phi = 24°$, and the CA-GB angle is $\Phi = -66°$ as indicated by the double arrow in b). Nearly perpendicular dislocations are present in the PFZs of both grains. The WBDF image in a) was acquired under $\vec{g} - 3\vec{g}$ conditions, using the $\vec{g} = [020]$ reflection of the left-hand side grain as indicated by the inset electron diffraction pattern. Note that the inset electron diffraction pattern was acquired in a [100] zone axis, before tilting the specimen and electron beam to $\vec{g} - 3\vec{g}$ conditions required for WBDF imaging as explained in the Materials section. This tilting also caused the GB plane to become inclined to the electron beam. The $\vec{g} \cdot \vec{b} = 0$ condition for dislocations "b1" and "b2" is satisfied for $\vec{g} = [0\bar{2}2]$ and $\vec{g} = [0\bar{2}\bar{2}]$, respectively. The BF TEM image in b) shows a larger view of the GB, with a particle labelled "P" as a reference to the WBDF image. No significant misorientation angles can be seen in the map presented in c). The GB plane is shown as a thin grey line. Note that images b) and c) were acquired with the GB plane edge on to the electron beam. Pole figures of the (100), (110), and (111) poles are given in d), where 86522 and 103809 data points are included for the left-hand and right-hand sides respectively.
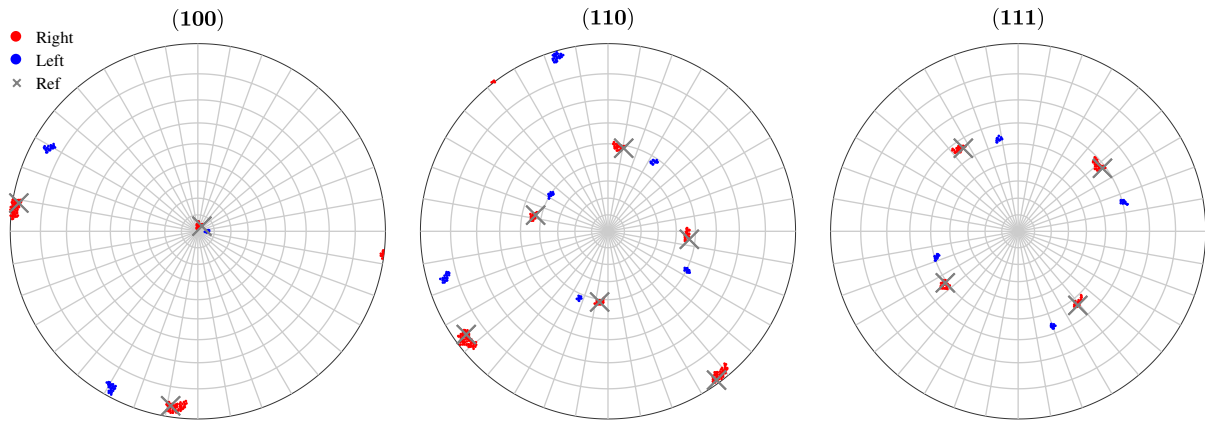
11
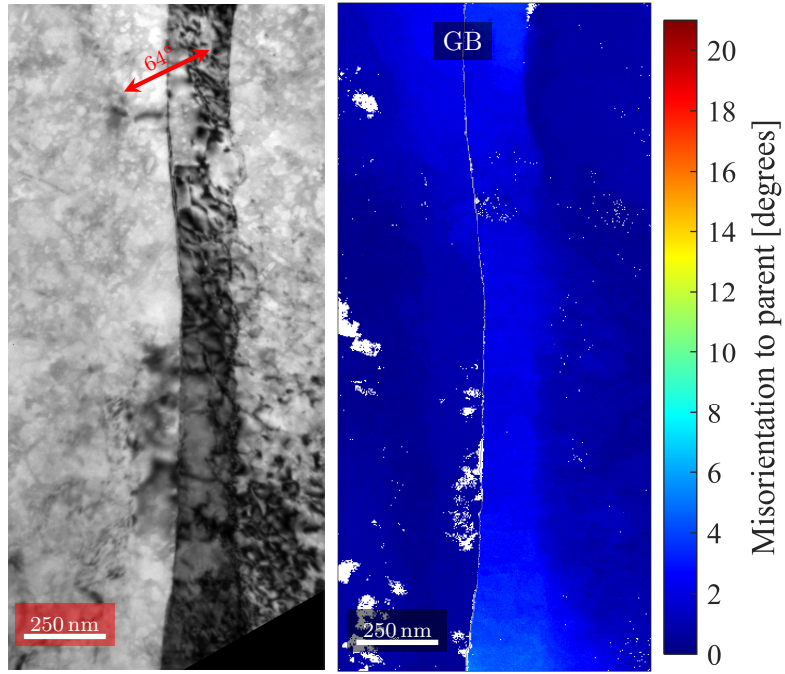
Figure 6: GB with dislocation *wall* at the PFZ boundary in one of the grains. The parent-parent misorientation is $\phi = 21°$, and the CA-GB angle is $\Phi = 64°$ as indicated by the double arrow in a). A dislocation wall, i.e., a *wall* feature, is seen at the boundary of the right-hand side PFZ in the BF TEM image shown in a). In b) the misorientation angles in degrees of each grain are shown, and the *wall* feature of the right-hand side PFZ corresponds to misorientations 2° to 3°. The GB plane is shown as a thin grey line. Pole figures of the (100), (110), and (111) poles are given in c), where 80514 and 107070 data points are included for the left-hand and right-hand sides respectively. The parent orientation of the right-hand side grain is marked by a cross.
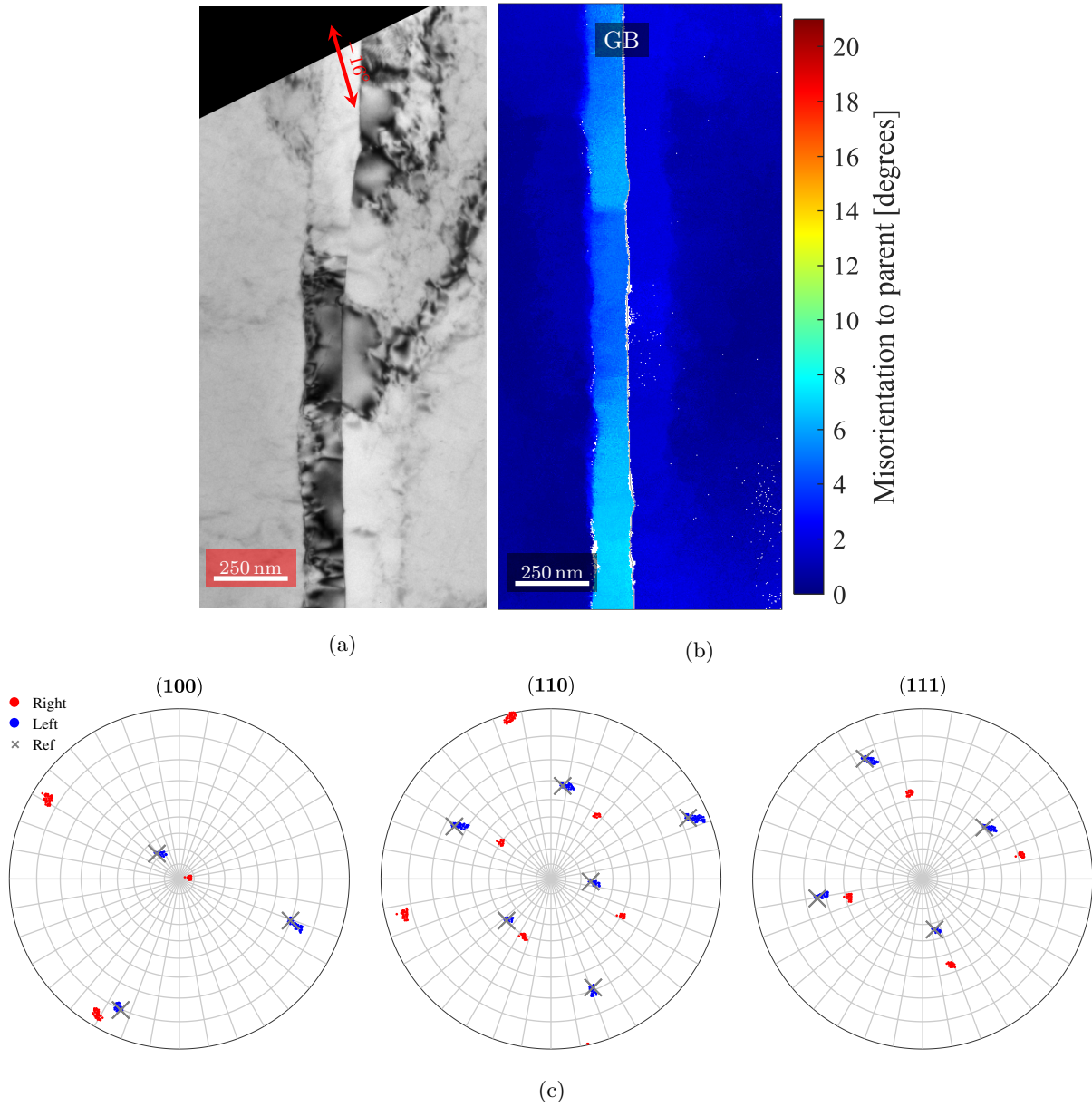
12

Figure 7: PFZs exhibiting the *band* and *wall* feature. The parent-parent misorientation is $\phi = 28°$, and the CA-GB angle is $\Phi = 16°$ as indicated by the double arrow in a). The BF TEM image in a) shows a band-like contrast in the left-hand side PFZ, while the contrast to the right of the GB is not as regular. In b) the misorientation angles in degrees of each grain are shown, and the band-like contrast of the left-hand side PFZ corresponds to misorientations 4.5° to 7°, which is labelled as a *band* feature. In the right-hand side PFZ, the misorientations indicate that a *wall* is present. The GB plane is shown as a thin grey line. Pole figures of the (100), (110), and (111) poles are given in c), where 86568 and 103610 data points are included for the left-hand and right-hand sides respectively. The parent orientation of the left-hand grain is marked by a cross.

13

a much larger orientation variation.

4. Discussion

The purpose of this study is to investigate how PFZs in a material behave when the material is deformed, with special emphasis on strain and crystal orientations. Based on the results obtained, it is clear that some PFZs can develop significantly different orientations than their parent grains, while others do not. PFZs may develop *dislocations*, *walls*, *bands*, or *grains*.

Regarding the *grains* that can form in PFZs, it should be noted that the orientation mapping algorithm can be somewhat misleading when it comes to the sizes of the grains. First of all, due to the phosphorescent screen and the resulting afterglow, any given pixel in the SPED data will consist of a mix of the PED pattern in that pixel and the previous pixels. This may cause problems when indexing the orientations, and boundaries between neighbouring grains tend to smear out in the fast scan direction. Secondly, if grains are overlapping, the indexing algorithm will tend to favour one of the orientations. This will occur at GBs inclined to the beam direction and influence the apparent sizes and shapes of the grains. However, when comparing the orientation maps with the TEM images, it becomes clear that the amount of overlap is limited, and the shapes and sizes of the grains in the orientation maps are qualitatively correct.

The features observed here are similar to results published by Jain [16], Styczyńska *et al* [15], Khadyko *et al* [18], and Schwellinger [4]. Jain [16] observed PFZ microstructures similar to *dislocations* and *walls* in his overaged Al-Mg-Si alloy subjected to cyclic loading. His results indicate that many more cycles are necessary for the *wall* feature to form than for the *dislocations*. The *in situ* experiments by Styczyńska *et al* [15] show that dislocations start by bowing out from the GB into the PFZ as half-loops at very low strains. These half-loops are pinned by precipitates at the PFZ boundary, and look similar to the *dislocations* feature. The strain that was required for these half-loops to form in the *in situ* study was very low, and only a few PFZs contained them, while other PFZs were unaffected by deformation. Further deformation caused dislocations to gather along the PFZ edge, similar to the *walls* in the present work. The study by Khadyko *et al* [18] considered the same alloy and heat treatment as the present study, but under tension rather than compression. *Dislocations* were observed both inside and outside the neck of the specimens, while *walls* were only observed inside the neck. Additionally, *bands* were sometimes also seen inside the neck, but less often than *walls*. These three reports indicate that *walls* and *bands* require higher strains in order to form, compared to *dislocations*. The only previous report of features similar to *grains* known to the authors, is the one by Schwellinger [4]. In the present work, *grains* were only observed in specimens compressed to 20% engineering strain or more, and they seemed more frequent in specimens compressed to 50% engineering strain. We therefore suggest that the density of PFZ *grains* increases with increasing strain.

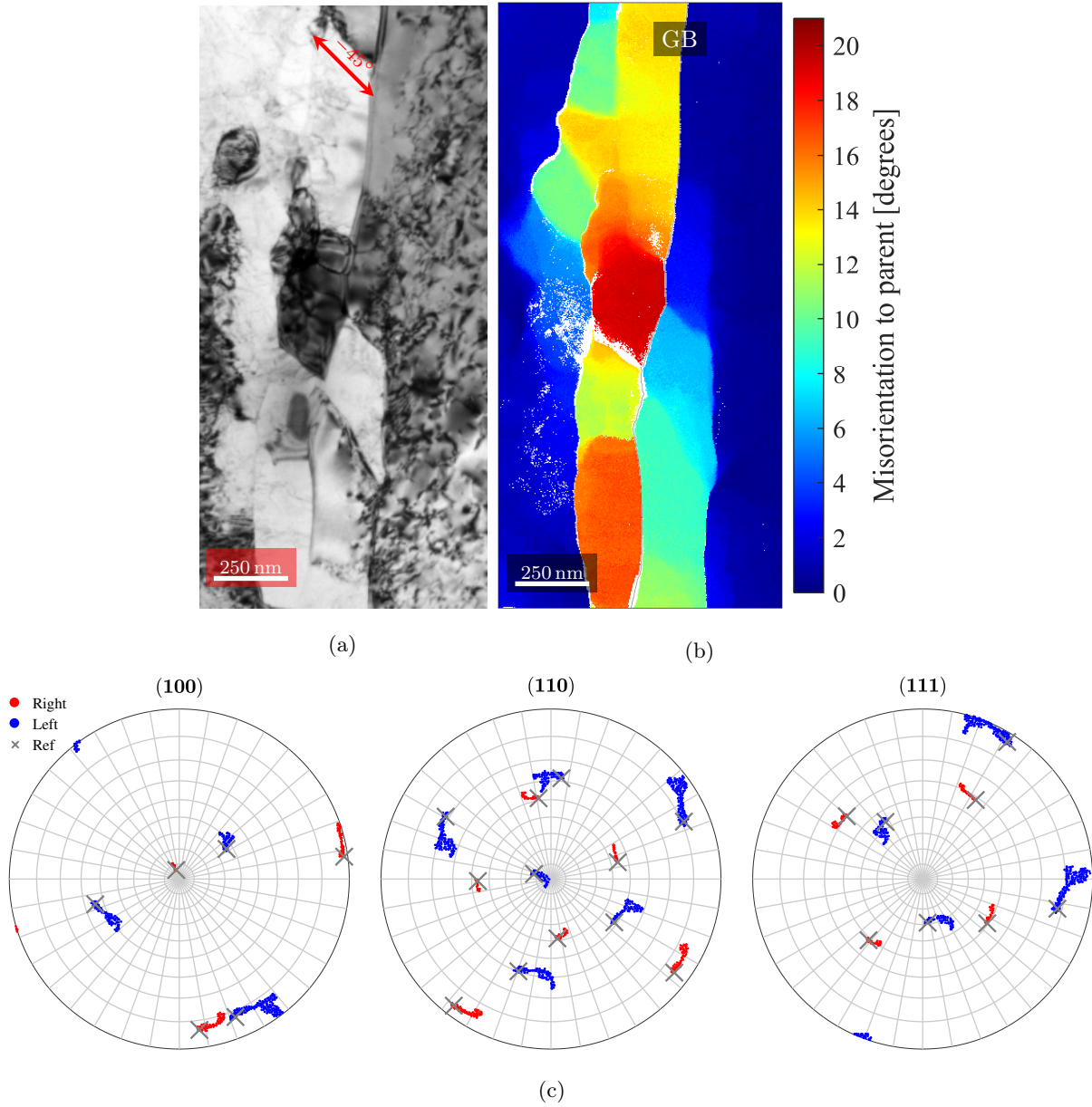A full and rigorous discussion on the mechanisms responsible for each feature is out of scope of the

Figure 8: PFZ with small regions of high misorientations relative to parent grain orientations, i.e. *grains*, observed by BF TEM and SPED orientation mapping. The parent-parent misorientation is $\phi = 38°$, and the CA-GB angle is $\Phi = 45°$ as indicated by the double arrow in a). The PFZ to either side of the GB has formed regions of different contrast in the BF TEM image shown in a). In b), the misorientation angles in degrees of each grain are shown. The GB plane is shown as a thin grey line. Pole figures of the (100), (110), and (111) poles are given in c), where 103805 and 82316 data points are included for the left-hand and right-hand sides respectively. The parent orientation of the two grains are marked by crosses.

current work. However, a brief discussion on the evolution of the features is given. Based on our and previous results it is reasonable to assume that the local strain around GBs determines what PFZ feature is formed at each particular GB. If a GB is subjected to low local strains, *dislocations* are formed, while for larger strains, *walls*, *bands*, or *grains* are formed. Because the local strain required for *walls* is lower than what is required for *bands*, it follows that each feature develops from another. As very low strains are required for *dislocations*, this is the first feature to form in any PFZ. When the global strain increases, so does the local strain, and eventually the *walls* feature may form where the local strains are large enough. Similarly, *bands* will also form once the local strain reaches some critical value. We therefore propose the following: during straining, dislocations are emitted as loops from the GBs and are pinned by precipitates at the outer edges of the PFZ, and all PFZs develop *dislocations* initially. As the deformation continues and GBs experience different stress and strain states, some PFZs develop *walls* due to many dislocations emitting from the GB and forming tangles among the precipitates in the PFZ transition region. This is supported by other studies as well [15, 16]. Upon further straining, some of these *walls* progress and develop into *bands*. As strain concentrates yet further at some GBs, the soft PFZ must form small grains in order to maintain compatibility with the harder grain interior and the neighbouring grain. It is clear that significant strains are required to form the large misorientations related to *grains*. Because some GB PFZs develop *dislocations*, while others develop *grains*, there must be large differences in local strains in GB PFZs in peak-aged AA6060.

The angle between the deformation axis and the GB plane is one parameter that has proven to influence the localisation of strain in PFZs [8, 18, 31], and this angle will then influence which features form at the different PFZs at a given global strain. For example, the only case of PFZ *grains* observed in this study occurred at a GB inclined 45° to the CA, which would result in maximum shear along the GB and large strain localisation in the PFZ. However, during deformation of a polycrystal, the individual grains will change shape and rotate, causing the angle between the CA and the GB planes to change. Therefore, a GB may pass through the 45° orientation and strain may localise before the GB rotates away from this critical orientation. It is therefore difficult to perform systematic studies on the importance of this parameter. The other features seem to form with no clear dependence on the CA orientation.

The effect of the observed PFZ features on material properties is challenging to establish. The work hardening in most PFZs is limited, since most PFZs exhibit the *dislocations* feature which corresponds to low dislocation densities compared to their parent grain. Some models, e.g. the one used by Pardoen *et al* [11], assumes extensive work hardening potential in PFZs. Such models will not be valid for most PFZs in peak-aged AA6060. On the other hand, the other three features will provide additional barriers for dislocation movement, and lead to a modified work hardening behaviour.

Perhaps most interesting, is the effect of *grains* on the PFZ strength. Assuming the PFZ behaves as a polycrystal consisting of grains with diameter $d \approx w$, a Hall-Petch type of approach is reasonable. When a

general polycrystal deforms, dislocations slipping on the same slip plane will pile-up against grain boundaries which act as dislocation motion barriers. The shear stress in front of a pile-up increases linearly with the number of dislocations, and the applied shear stress. Once enough dislocations have piled-up to initiate slip in the neighbouring grain, the frontmost dislocation may transmit to the other grain. However, if the grains in the polycrystal are small, there will be a limited number of dislocations that can fit inside each grain. Because of this, a higher stress must be applied in order to transmit dislocations across grain boundaries. This will strengthen the material, and leads to the so-called Hall-Petch grain boundary strengthening mechanism expressed by $\sigma_{HP} = \sigma_0 + k/\sqrt{d}$ [32, 33]. In the Hall-Petch relation, σ_0 is the friction stress, k is a constant describing the strength of the boundaries, and d is the grain diameter of the material. An identical relationship is applicable for materials with small cells separated by dislocation walls [9]. For aluminium alloys, k is in the range ~ 0.01 - 0.3 MPa$\sqrt{\text{m}}$, depending on the nature of the boundaries and/or cell walls [9, 34]. In the case of PFZ *grains*, the number of dislocations that may pile-up inside a single PFZ grain is very limited, and the strength of the PFZ should increase. Assuming that the PFZ is completely drained of solute, the friction stress of the PFZ is equal to the flow stress of high purity aluminium, i.e. $\sigma_0 \approx 11$ MPa [35]. Figure 9 shows how σ_{HP} changes as a function of d for different values of k. Approximating the PFZ *grains* as spherical grains, the equivalent diameters of the different grains present in the PFZs shown in Fig. 8b were also calculated and are plotted for reference. It is obvious that for weak boundaries, i.e. $k < 0.1$ MPa$\sqrt{\text{m}}$, the strength of the PFZ is much lower than the flow stress of the alloy. However, for $k \geq 0.1$ MPa$\sqrt{\text{m}}$, the strength of the PFZ will be comparable to the grain interior. The important point in this analysis is the fact that PFZs with *grains* may become stronger than the grain interior. This will cause dislocations approaching from the grain interior to pile-up against the PFZ. As a result, PFZ *grains* will screen the GB from pile-ups and will thus inhibit void nucleation at the GB. On the other hand, Schwellinger [4] suggested that large dislocation densities at the PFZ boundaries could provide locations for void nucleation through vacancy condensation, especially when impinged by slip bands from the grain interiors. Recent work on pure tantalum suggests that dislocation structures formed during deformation, rather than pre-existing GBs, are preferred sites for voids as well [14]. It should be noted, however, that very large local stresses would be required for voids to nucleate purely through plasticity and whether or not this may occur at the PFZ boundary will depend on whether the material favours planar slip. Thus, while PFZ *grains* might screen GBs from pile-ups and inhibit void nucleation, dislocation pile-ups at PFZ boundaries might nucleate voids there instead.

The different PFZ features found in the present work should be considered when designing models and simulations. Further work should include experimental investigations of whether the same features appear in alloys with different strengths and PFZ widths, as well as simulations of the impact of these features on material properties.

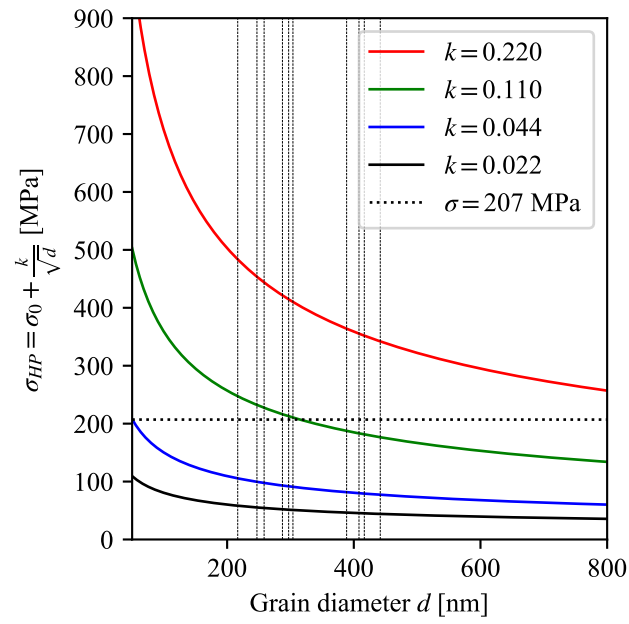Finally, it should be noted that the thin foil preparation of the specimens might have influenced the

Figure 9: Plot of Hall-Petch strengthening of polycrystalline aluminium σ_{HP} as a function of grain diameter d for different grain boundary diffusivity parameters k. The unit of k is MPa$\sqrt{\text{m}}$ and has been omitted from the legend for clarity. Vertical dashed lines indicate measured equivalent diameters of grains observed in the PFZs in Fig. 8b, while the horizontal dotted line show the flow stress of the bulk material [28].

microstructure. Especially dislocations originally present within PFZs might have escaped as a result of the thinning process. Therefore, the dislocation density in PFZs exhibiting *dislocations* may be higher than observed in the present work. However, it is unlikely that the sample preparation has altered the original microstructure of the *grains* feature markedly.

5. Conclusions

A detailed TEM and SPED orientation mapping study of four different HAGBs in the AA6060 aluminium alloy in peak aged condition compressed by 20% engineering strain has been performed along with a more general BF TEM study of specimens compressed to 5%, 10%, 20% and 50%. The results show that different PFZs in the same material can develop significantly different crystal orientations than their parent grains. We also show that in regions where such orientation differences do not form, the dislocation density inside the PFZ is much smaller than inside the grains. Four different microstructural features can be used to describe PFZs in the deformed state. These are "perpendicular dislocations" that span the PFZs, dislocation "walls" along the PFZ/bulk transition regions, PFZ "misorientation bands", and PFZ "grains", labelled as *dislocations*, *walls*, *bands*, and *grains*, respectively. A PFZ with *dislocations* tends to contain sets of dislocations parallel to each other, all showing large angles to the GB interface. *Walls* are characterized by relatively small misorientation ($\sim 3°$) between PFZ and parent grain. PFZ *bands* are similar to *walls*, but have a higher misorientation (between 4.5° and 7°) relative to their parent grain. PFZ *grains* are misoriented between 12° and 20° from their parent grain, and are separated from each other by LAGBs. The different features have been observed before, but the misorientations have not been quantitatively studied in detail. Based on the current investigation and reports from the literature, it is suggested that the features develop from each other during deformation. *Dislocations* appear in PFZs at small strains, but at larger strains, *walls* at the transition region between the PFZ and the grain interior may form. Further deformation results in PFZ *bands*. Finally, PFZ *grains* form at large strains. The local environment of the individual PFZ, including the angle between CA and GB, GB misorientation angle, and the orientation of each grain relative to the CA, is assumed to influence the global strain required to form each feature at a particular GB PFZ. GBs oriented close to 45° to the loading axis are suggested to form PFZ *grains* earlier than other GBs. Future works should investigate the impact of these PFZ features on material properties, and whether these features occur in other alloys with different strengths and PFZ widths.

Acknowledgements

Data availability

The raw data required to reproduce these findings cannot be shared at this time due to legal or ethical reasons. The processed data required to reproduce these findings cannot be shared at this time due to legal or ethical reasons.

References

[1] N. Ryum, The influence of a precipitate-free zone on the mechanical properties of an Al-Mg-Zn alloy, Acta Metallurgica 16 (3) (1968) 327–332. `doi:10.1016/0001-6160(68)90018-7`.

[2] M. Abe, K. Asano, A. Fujiwara, Influence of the precipitate-free zone width on the tensile properties of an Al-6 Wt pct Zn-1.2 Wt pct Mg alloy, Metallurgical Transactions 4 (6) (1973) 1499–1505. `doi:10.1007/BF02668000`.

[3] T. Kawabata, O. Izumi, Ductile fracture in the interior of precipitate free zone in an Al-6.0%Zn-2.6%Mg alloy, Acta Metallurgica 24 (9) (1976) 817–825. `doi:10.1016/0001-6160(76)90048-1`.

[4] P. Schwellinger, Investigation of the Mechanisms of Ductile Intergranular Fracture in Al-Mg-Si Alloys with Special Reference to Void Formation, Zeitschrift für Metallkunde 71 (8) (1980) 520–524.

[5] A. K. Vasudévan, R. D. Doherty, Grain boundary ductile fracture in precipitation hardened aluminum alloys, Acta Metallurgica 35 (6) (1987) 1193–1219. `doi:10.1016/0001-6160(87)90001-0`.

[6] P. N. T. Unwin, G. W. Lorimer, R. B. Nicholson, The origin of the grain boundary precipitate free zone, Acta Metallurgica 17 (11) (1969) 1363–1377.

[7] R. B. Nicholson, G. Thomas, J. Nutting, The interaction of dislocations and precipitates, Acta Metallurgica 8 (3) (1960) 172–176.

[8] T. F. Morgeneyer, M. J. Starink, S. C. Wang, I. Sinclair, Quench sensitivity of toughness in an Al alloy: Direct observation and analysis of failure initiation at the precipitate-free zone, Acta Materialia 56 (12) (2008) 2872–2884. `doi:10.1016/j.actamat.2008.02.021`.

[9] E. Huskins, B. Cao, K. Ramesh, Strengthening mechanisms in an Al–Mg alloy, Materials Science and Engineering: A 527 (6) (2010) 1292–1298. `doi:10.1016/j.msea.2009.11.056`.

[10] T. Pardoen, D. Dumont, A. Deschamps, Y. Brechet, Grain boundary versus transgranular ductile failure, Journal of the Mechanics and Physics of Solids 51 (4) (2003) 637–665. `doi:10.1016/S0022-5096(02)00102-3`.

[11] T. Pardoen, T. J. Massart, Interface controlled plastic flow modelled by strain gradient plasticity theory, Comptes Rendus Mecanique 340 (2012) 247–260. `doi:10.1016/j.crme.2012.02.008`.

[12] R. N. Gardner, T. C. Pollock, H. G. F. Wilsdorf, Crack initiation at dislocation cell boundaries in the ductile fracture of metals, Materials Science and Engineering 29 (2) (1977) 169–174. `doi:10.1016/0025-5416(77)90123-9`.

[13] H. G. F. Wilsdorf, The ductile fracture of metals: A microstructural viewpoint, Materials Science and Engineering 59 (1) (1983) 1–39. `doi:10.1016/0025-5416(83)90085-X`.

[14] P. Noell, J. Carroll, K. Hattar, B. Clark, B. Boyce, Do voids nucleate at grain boundaries during ductile rupture?, Acta Materialia 137 (2017) 103–114. `doi:10.1016/j.actamat.2017.07.004`.

[15] M. Styczyńska, W. Łojkowski, Grain boundaries as dislocation sources in a material with precipitate-free zones, Scripta Metallurgica 19 (12) (1985) 1409–1413. `doi:10.1016/0036-9748(85)90141-3`.

[16] M. Jain, TEM study of microstructure development during low-cycle fatigue of an overaged Al-Mg-Si alloy, Journal of Materials Science 27 (2) (1992) 399–407. `doi:10.1007/BF00543929`.

[17] C. Watanabe, R. Monzen, K. Tazaki, Effects of Al_3Sc particle size and precipitate-free zones on fatigue behavior and dislocation structure of an aged Al–Mg–Sc alloy, International Journal of Fatigue 30 (2008) 635–641. `doi:10.1016/j.ijfatigue.2007.05.010`.

[18] M. Khadyko, C. D. Marioara, I. G. Ringdalen, S. Dumoulin, O. S. Hopperstad, Deformation and strain localization in polycrystals with plastically heterogeneous grains, International Journal of Plasticity 86 (2016) 128–150. `doi:10.1016/j.ijplas.2016.08.005`.

[19] E. F. Rauch, M. Véron, Automated crystal orientation and phase mapping in TEM, Materials Characterization 98 (2014) 1–9. `doi:10.1016/j.matchar.2014.08.010`.

[20] R. Vincent, P. A. Midgley, Double conical beam-rocking system for measurement of integrated electron diffraction intensities, Ultramicroscopy 53 (3) (1994) 271–282. `doi:10.1016/0304-3991(94)90039-6`.

[21] J. S. Barnard, D. N. Johnstone, P. A. Midgley, High-resolution scanning precession electron diffraction: Alignment and spatial resolution, Ultramicroscopy 174 (2017) 79–88. `doi:10.1016/j.ultramic.2016.12.018`.

[22] I. Kovács, J. Lendvai, E. Nagy, The mechanism of clustering in supersaturated solid solutions of $A1-Mg_2Si$ alloys, Acta Metallurgica 20 (7) (1972) 975–983. `doi:10.1016/0001-6160(72)90092-2`.

[23] G. A. Edwards, K. Stiller, G. L. Dunlop, M. J. Couper, The precipitation sequence in Al–Mg–Si alloys, Acta Materialia 46 (11) (1998) 3893–3904. `doi:10.1016/S1359-6454(98)00059-7`.

[24] K. Matsuda, Y. Sakaguchi, Y. Miyata, Y. Uetani, T. Sato, A. Kamio, S. Ikeno, Precipitation sequence of various kinds of metastable phases in Al-1.0mass% Mg_2Si-0.4mass% Si alloy, Journal of Materials Science 35 (1) (2000) 179–189. `doi:10.1023/A:1004769305736`.

[25] C. D. Marioara, S. J. Andersen, H. W. Zandbergen, R. Holmestad, The influence of alloy composition on precipitates of the Al-Mg-Si system, Metallurgical and Materials Transactions A 36 (13) (2005) 691–702. `doi:10.1007/s11661-005-1001-7`.

[26] S. J. Andersen, H. W. Zandbergen, J. Jansen, C. Træholt, U. Tundal, O. Reiso, The crystal structure of the β" phase in Al-Mg-Si alloys, Acta Materialia 46 (9) (1998) 3283–3298. `doi:10.1016/S1359-6454(97)00493-X`.

[27] S. Wenner, R. Holmestad, Accurately measured precipitate-matrix misfit in an Al-Mg-Si alloy by electron microscopy, Scripta Materialia 118 (2016) 5–8. `doi:10.1016/j.scriptamat.2016.02.031`.

[28] B. H. Frodal, K. O. Pedersen, T. Børvik, O. S. Hopperstad, Influence of pre-compression on the ductility of AA6xxx aluminium alloys, International Journal of Fracture 206 (2) (2017) 131–149. `doi:10.1007/s10704-017-0204-4`.

[29] S. J. Andersen, Quantification of the Mg_2Si β" and β' phases in AlMgSi alloys by transmission electron microscopy, Metallurgical and Materials Transactions A 26 (8) (1995) 1931–1937. `doi:10.1007/BF02670664`.

[30] F. Bachmann, R. Hielscher, H. Schaeben, Grain detection from 2d and 3d EBSD data—Specification of the MTEX algorithm, Ultramicroscopy 111 (12) (2011) 1720–1733. `doi:10.1016/j.ultramic.2011.08.002`.

[31] G. Lütjering, J. Albrecht, C. Sauer, T. Krull, The influence of soft, precipitate-free zones at grain boundaries in Ti and Al alloys on their fatigue and fracture behavior, Materials Science and Engineering: A 468-470 (2007) 201–209. `doi:10.1016/j.msea.2006.07.168`.

[32] E. O. Hall, The Deformation and Ageing of Mild Steel: III Discussion of Results, Proceedings of the Physical Society. Section B 64 (9) (1951) 747–753. `doi:10.1088/0370-1301/64/9/303`.

[33] R. Armstrong, I. Codd, R. M. Douthwaite, N. J. Petch, The plastic deformation of polycrystalline aggregates, Philosophical Magazine 7 (73) (1962) 45–58. `doi:10.1080/14786436208201857`.

[34] A. Loucif, R. B. Figueiredo, T. Baudin, F. Brisset, R. Chemam, T. G. Langdon, Ultrafine grains and the Hall–Petch relationship in an Al–Mg–Si alloy processed by high-pressure torsion, Materials Science and Engineering: A 532 (2012) 139–145. `doi:10.1016/J.MSEA.2011.10.074`.

[35] I. Polmear, Light Alloys, Butterworth-Heinemann, 2005.